Assessing the Potential of the MTG-FCI Geostationary Mission for the Detection of Methane Plumes

Shanyu Zhou[a,*], Javier Gorroño[a], Javier Roger[a], Itziar Irakulis-Loitxate[a,b], Rasmus Lindstrot[c], Zhipeng Pei[d], Lulu Si[a], and Luis Guanter[a,e]

[a]Research Institute of Water and Environmental Engineering (IIAMA), Universitat Politècnica de València, València, Spain
[b]International Methane Emissions Observatory, United Nations Environment Program, Paris, France
[c]EUMETSAT, Darmstadt, Germany
[d]State Key Laboratory of Information Engineering in Surveying, Mapping and Remote Sensing, Wuhan University, Wuhan, China
[e]Environmental Defense Fund, Amsterdam, The Netherlands
[*]szhou1@upv.es

June 2025

This is a non-peer-reviewed preprint submitted to EarthArXiv, submitted to peer review at Environmental Science & Technology.

Abstract

The Flexible Combined Imager on the Meteosat Third Generation (MTG-FCI) provides geostationary observations over Europe and Africa, the Middle East, and parts of South America, and the surrounding waters. The FCI samples the visible, near-infrared and shortwave infrared spectral windows with a spatial resolution at nadir between 500 and 1000 m, and a 10-min temporal sampling. This configuration offers potential for methane retrievals using Multi-Band Multi-Pass retrieval (MBMP) methods, as shown with other multispectral missions. The potential of the MTG-FCI system for the detection and monitoring of single methane plumes is evaluated in this paper through different approaches. End-to-end simulations using high-resolution WRF-LES methane plumes over Algeria showed that MTG-FCI can detect emissions as low as 30 t/h, where initial plume signals become visible, with clearer detection above 50 t/h. Additionally, mass-balance modeling estimated a minimum detection limit of 20–30 t/h across the central MTG-FCI disk (GSD $\leq$ 1 km) under optimal conditions. We illustrate the use of the MTG-FCI for the monitoring and quantification of methane plumes using a real transient emission detection from a compressor station in Algeria (34.676° N, 6.191° E) on September 29, 2023, capturing its full evolution from 10:40 to 15:50 UTC. The estimated emission rate of 353 $\pm$ 78 t/h aligns with independent estimates from other satellites. These results highlight MTG-FCI's ability to track large methane plumes in near real-time, complementing polar-orbiting sensors.

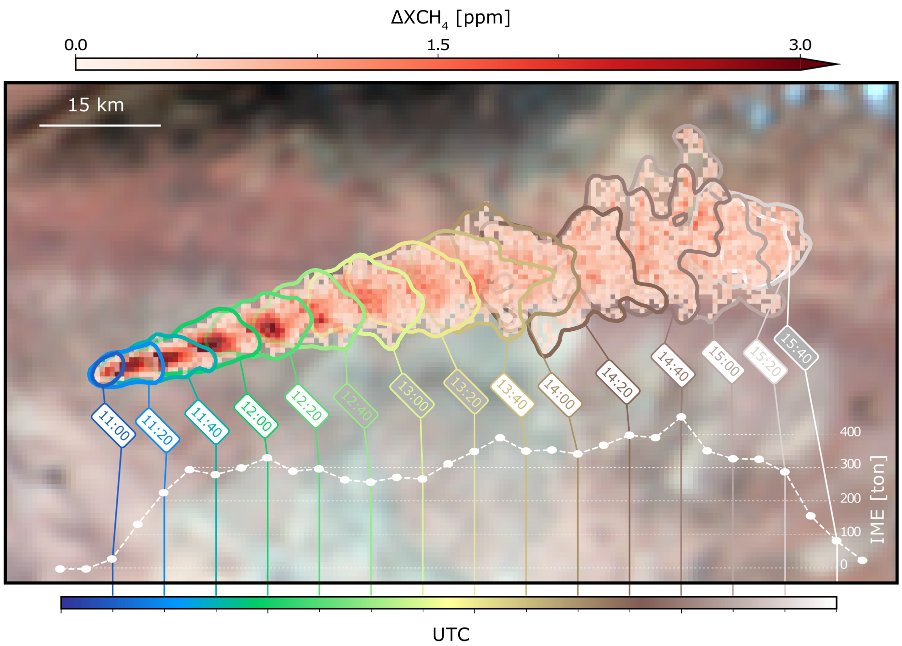

Keywords: MTG-FCI, Methane Plume Detection, Earth Observation, Geostationary Remote Sensing

1 Introduction

Methane (CH_4) is a potent greenhouse gas with a global warming potential (GWP) approximately 86 times greater than carbon dioxide (CO_2) over a 20-year period (Myhre et al., 2013). Despite its relatively short atmospheric lifetime of about nine years (Etminan et al., 2016), methane substantially contributes to climate change due to its strong radiative forcing effect. Rapid reductions in methane emissions can lead to near-term climate benefits (Shindell et al., 2012). Anthropogenic methane emissions primarily originate from the oil and gas (O&G) industry, agriculture, and waste management (Schwietzke et al., 2016; Saunois et al., 2020). Among these, O&G emissions, often occurring as super-emissions from discrete point sources, present a promising target for mitigation due to the availability of cost-effective reduction strategies (UNEP, 2021).

The detection and quantification of large methane emissions from point sources have been significantly enhanced by satellite-based remote sensing spectrometers sampling the 1600-2500 spectral window with a continuous spectral sampling. The TROPOspheric Monitoring Instrument (TROPOMI) aboard Sentinel-5 Precursor provides daily global coverage, facilitating the identification of large methane plumes around the globe (Veefkind et al., 2012). High-resolution instruments such as GHGSat offer more localized monitoring of methane emissions (Varon et al., 2019). Furthermore, hyperspectral missions such as EMIT, PRISMA and EnMAP allow for refined methane detection using advanced spectral analysis (Guanter et al., 2021; Thorpe et al., 2023; Roger et al., 2024).

Multispectral missions offer an alternative approach for methane detection by utilizing a limited number of discrete spectral bands with sensitivity to methane absorption. Instruments such as the Sea and Land Surface Temperature Radiometer (SLSTR) aboard Sentinel-3, the Visible Infrared Imaging Radiometer Suite (VIIRS) on the Suomi National Polar-orbiting Partnership (Suomi-NPP) and Joint Polar Satellite System (JPSS) - also known as NOAA-20 and NOAA-21 - satellites, and the Multispectral Imager (MSI) on Sentinel-2 have demonstrated potential in detecting methane emissions through analysis of near-infrared (NIR) and shortwave infrared (SWIR) reflectance variations (Pandey et al., 2023; Thorpe et al., 2017; Ehret et al., 2022; Varon et al., 2021; de Jong et al., 2025). These sensors operate in sun-synchronous orbits, providing global coverage with revisit times that exhibit considerable variation. Sentinel-3A and Sentinel-3B, for instance, achieve a combined revisit time of less than one day at the equator, whereas Sentinel-2A and Sentinel-2B revisit the same location approximately every five days at the equator and more frequently at higher latitudes. In contrast to these instruments, TROPOMI offers daily global coverage with higher methane sensitivity, making it particularly suited for monitoring large-scale emission patterns. However, the detection capabilities of these sensors are constrained by factors such as cloud cover (Ehret et al., 2022), surface reflectance variations (Varon et al., 2021), and relatively coarse spectral resolution compared to hyperspectral instruments, leading to a lower sensitivity to methane for multispectral sensors (Gorroño et al., 2023). Despite their effectiveness, these satellites operate in low Earth orbit, limiting their frequency of re-visit and thus restricting their ability to fully monitor transient emissions (Qu et al., 2021).

Regarding temporal resolution, the best performance is the one offered by geostationary satellites such as the Advanced Baseline Imager (ABI) aboard the GOES satellite series, which provides continuous monitoring of the Americas at 5- to 10-minute intervals with a ground sampling distance (GSD) of 1 to 2 km at nadir (Hall et al., 2023). The GOES-16 and GOES-17 satellites, primarily designed for weather and environmental monitoring, have demonstrated the capability to detect large methane emission events through reflected solar radiation in the SWIR and NIR channels. Recent studies have leveraged GOES-ABI data to detect methane plumes over North America, showing that geostationary observations can provide valuable insights into emission dynamics with unprecedented temporal coverage (Watine-Guiu et al., 2023), estimating a detection limit in the range of 10 to 100 tons per hour (t/h). This high-frequency observation capability allows for the identification of short-lived emission events, such as those associated with equipment malfunctions, gas venting, and blowouts in the O&G sector. However, the relatively coarse spatial resolution of GOES-ABI limits its ability to resolve smaller sources.

The Flexible Combined Imager on Meteosat Third Generation (MTG-FCI) represents a significant advancement in methane monitoring, offering high temporal resolution and broad spectral coverage from a geostationary orbit sampling Europe and Africa, the Middle East, and parts of South America, and the surrounding waters. The MTG-FCI captures data every 10 minutes in full disck and 2.5 minutes in Europe with a GSD of 0.5 to 1 km at nadir. Its spectral configuration includes multiple bands in the NIR and SWIR regions (Durand et al., 2015), encompassing methane-sensitive wavelengths, thereby enabling effective detection of methane enhancements. MTG-FCI is the first geostationary mission applicable for continuous regional methane monitoring across Europe and Africa, building upon the approach successfully applied to the GOES series over the Americas.

In this study, we investigate the potential of MTG-FCI for methane detection, focusing on retrieval performance and detection capability. We perform an end-to-end simulation over one of the most frequently observed methane emission regions in the UNEP's International Methane Emissions Observatory (IMEO) plume database, located in Algeria, using the multi-band multi-pass (MBMP) method to assess the instrument's capabilities. Furthermore, we estimate the theoretical minimum detectable methane emission rate across the full disk of MTG-FCI using empirical formulations (Jacob et al., 2016), accounting for key atmospheric and instrumental parameters. We illustrate the potential of the MTG-FCI for the detection and monitoring of transient methane plumes by analyzing a real emission event in Algeria on September 29, 2023.

2 Materials and Methods

2.1 MTG-FCI System

The FCI is an advanced imaging instrument deployed aboard the Meteosat Third Generation Imager (MTG-I) satellite (Holmlund et al., 2021). It is designed to provide high-resolution geostationary observations across multiple spectral domains. The instrument is equipped with 16 spectral bands spanning from the visible to the thermal infrared, enabling the monitoring of a wide range of atmospheric and surface phenomena within large parts of Europe and Africa, the Middle East, and parts of South America, and the surrounding waters. In particular, its spectral channels at 1.6 μm (NIR1.6) and 2.2 μm (NIR2.2) offer significant potential for methane emission detection. The NIR2.2 spectral channel is available in both the FDHSI (Full Disc High Spectral Resolution Imagery) configuration, with a central ground sampling distance (GSD) of 1000 m, and the HRFI (High Spatial Resolution Fast Imagery) configuration, which achieves a nadir GSD of 500 m. In contrast, the NIR1.6 spectral channel is recorded exclusively in FDHSI mode.

Figure 1 provides an overview of the spatial and spectral features of MTG-FCI relevant to methane detection. The first panel (Figure 1a) illustrates the approximate GSD of the HRFI configuration, which varies across the field of view due to the geostationary observation geometry. To account for the varying spatial resolution along and across the track, the effective GSD is estimated using the geometric mean of the latitudinal and longitudinal resolutions: $\mathrm{GSD} \approx \sqrt{\mathrm{dLat} \times \mathrm{dLon}}$, which provides a more representative measure of the pixel footprint under different viewing geometries. As shown in Figure 1b, the MTG-FCI effectively captures wavelengths that are highly sensitive to methane's spectral absorption features, with a finer spectral resolution than Sentinel-2's MSI. Notably, methane exhibits strong absorption at the band 2.2 μm, whereas the adjacent 1.6 μm band experiences minimal absorption. This contrast in absorption allows for methane concentration retrieval by leveraging surface reflectance similarities between the two bands. As a supplement to the Himawari and GOES geostationary series, MTG-FCI offers 10-minute temporal resolution for full disk coverage, and a significantly higher 2.5-minute resolution over Europe. The spectral, spatial, and temporal sampling of MTG-FCI makes it a very promising instrument for detecting, quantifying, and tracing methane plumes emitted from point sources, such as those originating in O&G extraction infrastructure or coal mining.

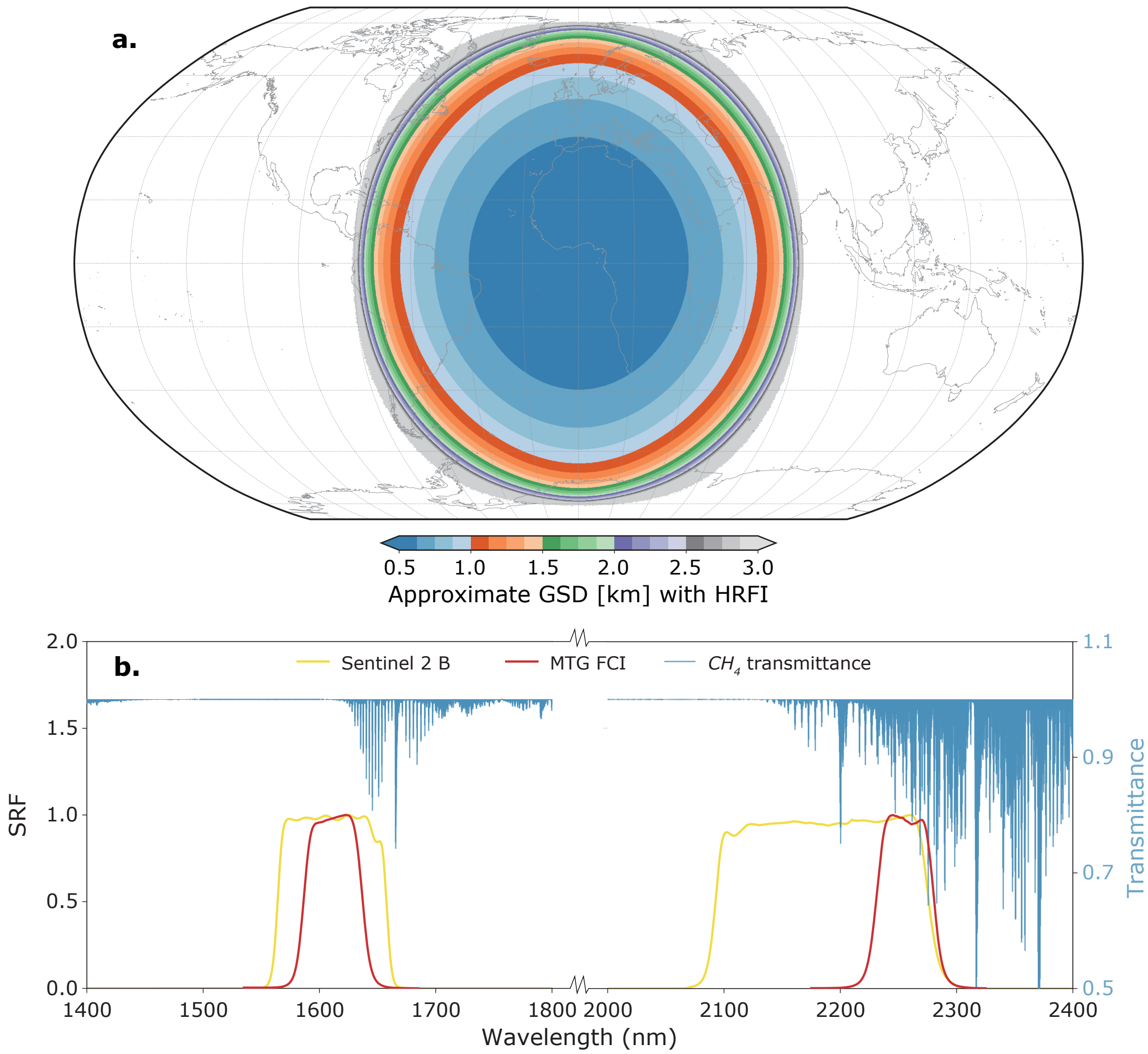

Figure 1: Overview of MTG-FCI spatial and spectral properties relevant for methane detection. (a) Approximate ground sampling distance (GSD) in kilometers for the HRFI configuration (NIR 22), illustrating spatial resolution variations across the field of view. (b) Averaged FCI Spectral Response Functions (SRF) of methane-related wavelength, Yellow curve: Sentinel-2B; Red curve: MTG-FCI; Blue lines: spectral sampling of the transmittance spectrum

2.2 Methane Retrieval

The retrieval framework developed for the GOES-ABI instrument (Watine-Guiu et al., 2023) and Sentinel-2/MSI (Gorroño et al., 2023) has served as a reference in designing the MTG-FCI retrieval scheme. In particular, the MBMP retrieval algorithm from Gorroño et al. (2023) has been adapted for MTG-FCI data, leveraging band ratios to isolate the methane absorption signal from surface reflectance variations. Specifically, the algorithm utilizes a methane-sensitive spectral channel centered at 2250 nm (NIR2.2 in MTG-FCI) alongside a reference channel at NIR1.6, which exhibits minimal methane absorption. To further mitigate surface-related artifacts, the band ratio from a given observation (containing a methane plume) is normalized against a corresponding ratio from a designated reference day (plume-free). Mathematically, this is expressed as:

$$T_{\text{plume}}(\lambda) \sim \frac{\rho}{\rho_{\text{ref}}} = \frac{\left(\frac{\rho_{\text{NIR}_{22}}}{\rho_{\text{NIR}_{16}}}\right)_{plume}}{\left(\frac{\rho_{\text{NIR}_{22}}}{\rho_{\text{NIR}_{16}}}\right)_{plume\text{-}free}} = e^{-\text{AMF}\cdot\sigma_{\text{CH}_4}(\lambda)\cdot\Delta X_{\text{CH}_4}} \tag{1}$$

where *plume* and *plume-free* refer to the presence and absence of methane plumes, respectively. ρ represents the top-of-atmosphere (TOA) radiance.

The retrieved transmittance, $T_{\text{plume}}(\lambda)$, is directly related to the methane concentration enhancement (ΔX_{CH_4}), through the air-mass factor (AMF) and methane absorption cross-section (σ_{CH_4}). To model methane's spectral transmittance and establish the relationship between atmospheric methane enhancement and absorption characteristics, a look-up table (LUT) was employed. This approach effectively accounts for atmospheric interactions and radiative transfer effects, ensuring accurate retrieval of methane enhancements.

Although some common principles were adopted from Sentinel-2 MBMP retrievals, such as the incorporation of multispectral and multitemporal information to enhance methane detection, the adaptation of the MTG-FCI introduced new challenges. While MTG-FCI offers a significantly higher temporal resolution than Sentinel-2, this advantage presents a distinct challenge: determining an effective temporal sampling strategy that balances redundancy avoidance with retrieval stability. Another challenge arises from differences in spatial resolution between the MTG-FCI NIR2.2 (0.5 km/1 km) and NIR1.6 (1 km) bands. Since spatial resolution directly influences the detection limits for ΔX_{CH_4}, using NIR2.2 data at its highest resolution (0.5 km) while incorporating multitemporal information provides advantages over directly pairing NIR2.2 and NIR1.6 at their resolution in FDHSI mode (1 km). To ensure spatial consistency, the NIR1.6 band was upsampled from 1 km to 0.5 km, aligning with the finer resolution of NIR2.2 and enhancing the accuracy of methane retrievals.

An additional challenge lies in minimizing surface-related artifacts to improve the robustness of methane retrieval. To ensure consistent illumination conditions, background data are selected from the closest available clear-sky day within one to two days of the target observation while maintaining the same observation time. For instance, if the methane-containing target data correspond to 11:00 UTC on September 29, 2023, the background is selected from the clearest available day at 11:00 UTC (e.g., September 28 or 30) by evaluating overall cloud-free conditions, ensuring consistent observation time. This approach minimizes diurnal variations in illumination and atmospheric conditions, enhancing the reliability of the methane signal extraction. It is also important to ensure that the selected days are free from rapid scene changes such as precipitation or intense human activity.

2.3 Detection and quantification of methane enhancements

Methane plume detection in this study is based on a thresholding technique, which employs a dual-threshold approach optimized for MTG-FCI observations. Specifically, pixels exceeding a predefined low threshold (e.g., $>2\sigma$, where σ refers to the retrieval standard deviation) are included in the plume mask only if they are spatially connected to pixels surpassing a higher threshold (e.g., the 95th percentile). To further refine the detection, we apply a 3×3 median filter to suppress high-frequency noise and visually adjust the mask in cases where atmospheric or sensor-induced artifacts are present.

To quantify the methane plume, we compute the Integrated Mass Enhancement (IME) (Frankenberg et al., 2016; Varon et al., 2018), which represents the excess mass of methane within the detected plume area. The IME is derived using the following equation, adapted for MTG-FCI's spatial and spectral characteristics:

$$\mathrm{IME} = M_{\mathrm{CH_4}} \sum_{j=1}^{N} \Delta\Omega_j A_j \tag{2}$$

$$\Delta\Omega_j = \frac{H_{\mathrm{col}} \cdot \Delta X_{CH_{4_j}}}{10^6 \times V_m} \tag{3}$$

where $M_{\mathrm{CH_4}} = 0.01604\,\mathrm{kg\ mol^{-1}}$ is the molar mass of methane, $A_j = x_{\mathrm{res}} \times y_{\mathrm{res}}\,(\mathrm{m^2})$ denotes the corresponding pixel area, N is the total number of pixels included in the mask. $\Delta\Omega_j(\mathrm{mol\ m^{-2}})$ represents the methane column enhancement in the j-th pixel. $H_{\mathrm{col}} = 8000\,\mathrm{m}$ is the assumed atmospheric column height, representing the vertical extent of methane enhancement considered in the calculation. $V_m = 0.0224\,\mathrm{m^3mol^{-1}}$ is the molar volume of an ideal gas under standard temperature and pressure. $\Delta X_{CH_{4_j}}$ (ppm) is the calculated methane concentration enhancement in the j-th pixel under the assumption of uniform dispersion within the H_{col}. To mitigate residual surface and background atmospheric biases, we introduce a temporal correction defined as:

$$\Delta X^{\mathrm{corr}}_{\mathrm{CH_4}} = \Delta X_{\mathrm{CH_4}}(t) - \Delta X_{\mathrm{CH_4}}(t_0) \tag{4}$$

Where $\Delta X_{\mathrm{CH_4}}(t)$ is the enhancement at time t, and $\Delta X_{\mathrm{CH_4}}(t_0)$ corresponds to the enhancement at a reference baseline time (here, 10:40 UTC). This correction is applied pixel-wise over the plume mask at each time step. This timestamp was selected because it immediately precedes the emission event and is not yet influenced by plume dispersion, while also minimizing uncertainties from inter-day radiance variability that could arise from using different days or observation geometries. This approach ensures that the corrected IME reflects the net methane signal attributable to the emission event, independent of residual surface or atmospheric biases present in the baseline frame.

2.4 Sensitivity analysis

2.4.1 End-to-End Simulation

To evaluate the capability of MTG-FCI in methane detection, an end-to-end simulation was conducted using realistic methane plume data derived from the Weather Research and Forecasting Large Eddy Simulation (WRF-LES model). Following the methodology previously applied to Sentinel-2 (Gorroño et al., 2023), the simulated methane plume was incorporated into the background image to assess retrieval performance and detection limits. The base imagery used to generate FCI-like simulated datasets was obtained from pre-operational MTG-FCI Level 1 data provided by European Organisation for the Exploitation of Meteorological Satellites (EUMETSAT).

The simulation process consists of several key stages. First, high-resolution methane mass distributions from the three-dimensional WRF-LES model were collapsed vertically into a 2D map and then spatially binned to match the MTG-FCI pixel grid, aligning with the instrument's spatial resolution. The binned methane data was then transformed into a two-dimensional methane enhancement image, simulating the plume as it would be observed from a satellite perspective. Using the precomputed LUT, the corresponding methane enhancement values were assigned to each pixel. Finally, to maintain consistency with actual MTG-FCI observations, the simulated dataset was then convolved with the instrument's Spectral Response Functions (SRF), aligning it with the sensor's radiometric properties.

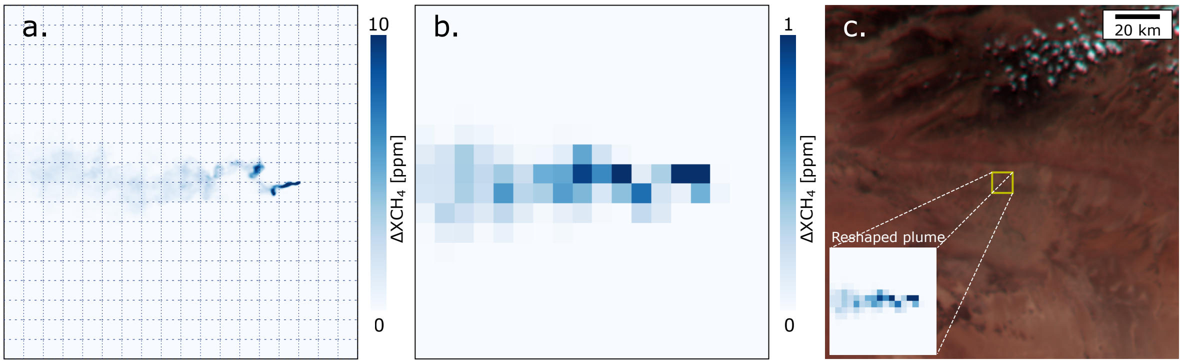

Figure 2: Methane enhancement map (ΔXCH_4) of the plumes used in the simulations, scaled to a flux rate of Q = 50 t/h after resampling to a 500 m resolution. (a) Original ΔXCH_4 map at 25-m spatial sampling in range 0-10 ppm, (b) Convolved ΔXCH_4 map in range 0-1 ppm, and (c) Schematic diagram of the simulation area overlaid on the MTG-FCI's RGB image.

Figure 2 depicts the transition from a high-resolution WRF-LES-generated methane plume (a) to the spatial configuration of MTG-FCI (b), highlighting the impact of spatial resampling on methane enhancement levels. In panel (a), the original plume, simulated with a GSD of 25 meters, exhibits fine-scale structures with localized enhancement levels reaching up to 10 ppm. However, after resampling to the 500m resolution of MTG-FCI (b), the methane enhancement levels are significantly reduced by approximately an order of magnitude across most of the area, making plume detection more challenging. Panel (c) provides a contextual view, showing the synthetic methane plume overlaid onto the real scene. The zoomed-in region demonstrates how the plume structure is reshaped at the coarser resolution, which covers an area of approximately 18×18 pixels, emphasizing the trade-off between spatial coverage and detection sensitivity in MTG-FCI observations.

2.4.2 Relative Detection Limit Estimation for Comparative Assessment

While end-to-end simulations can provide precise detection limits for specific times and locations, leveraging established empirical formulas offers a more efficient means of estimating methane detectability across the full MTG-FCI coverage area. Therefore, we adopt an approach based on existing parameterizations to estimate the minimum detectable methane emission rate (Q_{min}) across the MTG-FCI domain. For the FCI's NIR2.2 spectral channel, Q_{min} is primarily governed by key atmospheric and instrumental parameters. Following the formulation proposed by ?, the detection limit for a single pixel can be expressed as:

$$Q_{\text{min}} = M_{\text{CH}_4} \cdot U \cdot GSD \cdot q \cdot \sigma_{\Delta\text{XCH}_4} \tag{5}$$

where M_{CH_4} is the molar mass of methane, U represents the wind speed, $\sigma_{\Delta\text{XCH}_4}$ corresponds to the methane column precision, namely, the standard deviarion of the ΔX_{CH_4} estimation, and q is the number of standard deviations above the noise floor required for a confident detection. In this study, we adopt $q = 2$, a commonly used threshold in satellite-based methane detection limit studies (Jacob et al., 2016). The wind speed U is derived from the 10-meter wind speed (U_{10}) provided by the Global Wind Atlas (Davis et al., 2023), which offers a spatial resolution of 250 meters.

In practice, however, estimating $\sigma_{\Delta XCH_4}$ at the single-pixel level over large areas and multiple observation times poses substantial computational challenges due to the massive volume of data involved. To address this, we approximate the single-pixel methane column precision using the standard deviation calculated over a 300 × 300 pixel region. This spatially averaged estimate reduces the computational burden while still capturing representative variability within each region. While the Eq. 5 was originally derived at the pixel level, the use of regional standard deviation to approximate σ_{XCH_4} provides a practical and conservative estimate of the minimum detectable plume signal, assuming detection over small spatially connected areas.

Although we approximate the pixel-level methane column precision using statistics from a larger area (300 × 300 pixels), we still apply the GSD of a single-pixel in Eq. 5, not the aggregated scale of the larger area. This approach ensures our detection limit estimates reflect the sensor's native resolution at the pixel level, despite the noise approximation at a broader scale. The selected 300 × 300 pixel window corresponds to a region of approximately 150 km × 150 km at nadir. The estimation of $Q_{\min}$was based on observations collected at 13:30 UTC on three cloud-free days per month, spanning the period from September 2024 to February 2025 (see Section 2.6). For each 300 × 300-pixel region, the lowest $Q_{\min}$ value among all sampled days was selected to represent the best detection sensitivity achievable under typical observation conditions. In addition to the global assessment based on a 300 × 300-pixel grid, we also conducted finer-scale analyses using a 10 × 10-pixel moving window (approximately 5 km resolution) in key regions such as Hassi Messaoud, in order to better resolve spatial variations in detection capability at the plume scale. It should be noted that the estimated $Q_{\min}$ serves primarily as a comparative metric to assess relative methane detection potential across different regions and observation times, rather than an absolute indicator of true detection thresholds. In practice, detecting methane plumes generally requires coherent enhancements across multiple spatially connected pixels, a criterion not explicitly accounted for in Eq. 5.

2.5 Pre-processing

Before methane retrieval and quantification, preprocessing is essential to ensure accurate alignment of spectral bands and reliable cloud masking, reducing potential retrieval artifacts.

2.5.1 Co-registration

A crucial step in methane detection is ensuring precise spatial alignment across spectral bands (band-to-band) and across multiple observation dates (date-to-date) for accurate multispectral and temporal analysis. Accurate co-registration is critical for methane detection, as even minor misalignments can introduce significant errors in band ratios, as the ones included in the MBMP retrieval. Spatial offsets between bands may lead to artifacts in methane plume retrievals, impacting the accuracy of estimated methane concentrations. In this study, the NIR1.6 band was co-registered with the reference band NIR2.2 to maintain spatial consistency across all spectral channels. Given the difference in spatial resolution between these bands, NIR1.6 (1 km) was upsampled to match the higher resolution of NIR2.2 (0.5 km) before co-registration. This co-registration process was performed using GeFolki (Aplyer), an advanced image alignment tool based on the optical flow method. GeFolki was utilized to address specific spatial misalignment issues identified in pre-operational MTG-FCI data. Notably, discrepancies were observed between consecutive scans, leading to subtle shifts that could impact methane retrieval accuracy. Additionally, misalignments were detected between different spectral bands, further complicating precise co-registration. Unlike conventional linear or affine transformations, GeFolki's optical flow-based approach dynamically adjusts pixel positions based on intensity gradients, achieving sub-pixel alignment and reducing scan-related distortions for improved spectral consistency. The correction before and after is shown in the Supplementary video.

2.5.2 Cloud Screening

Following co-registration, cloud screening was applied to remove pixels contaminated by clouds, which can obscure surface reflectance and interfere with radiative transfer calculations. The cloud ratio (c) is derived from the ratio of IR10.5 (10.5 μm) and NIR0.4 (0.4 μm), defined as:

$$\mathrm{c} = \frac{\mathrm{IR105} - \mathrm{NIR04}}{\mathrm{IR105} + \mathrm{NIR04}} \tag{6}$$

Pixels below the 8th percentile threshold were classified as cloud-covered. The 8th percentile threshold was selected empirically and can be adjusted based on cloud detection performance to optimize the balance between excluding cloudy pixels and preserving clear-sky data. IR105, sensitive to thermal radiation, highlights cold cloud tops, while NIR04, reflective in the near-infrared, enhances cloud-surface contrast. To further ensure cloud contamination was minimized, cloud masks derived from MSG (Meteosat Second Generation) observations were used to validate the selection of cloud-free pixels, as this work was conducted during the commissioning phase of FCI. Superior cloud masking will be available from FCI operational products in future applications.

2.6 Satellite and Auxiliary Data

This study integrates multiple satellite and auxiliary datasets to ensure robust methane detection, retrieval, and validation. The primary dataset is obtained from the MTG-FCI instrument, which provides high-temporal-resolution imagery over Europe, Africa, the Middle East, and parts of South America. To complement these observations, additional datasets from VIIRS, WRF simulations, and reference databases were incorporated for validation, source attribution, and performance benchmarking.

VIIRS Observations The Visible Infrared Imaging Radiometer Suite (VIIRS), onboard Suomi-NPP, JPSS-1, and JPSS-2 (he latter two are also known as NOAA-20 and NOAA-21) satellites, provides 750 m nadir resolution radiance measurements. VIIRS SWIR bands M10 (1.6 μm) and M11 (2.2 μm), which are sensitive to methane absorption (de Jong et al., 2025), were used to detect methane plumes using the same MBMP retrieval framework as for MTG-FCI. Multiple VIIRS overpasses on September 29, 2023, were used for plume detection, with plume-free scenes from September 28 and 30 as reference. The preprocessing steps included Level 1B radiance extraction, spatial subsetting over the ROI, and reprojection for scene alignment.

Additional Data during Processing The WRF-LES simulated methane plumes were injected into real FCI backgrounds to conduct end-to-end sensitivity analysis. For both retrieval and simulation, cloud-affected pixels were excluded using a combined method: a reflectance ratio-based cloud mask (IR10.5/NIR0.4) and independent cloud flags from MSG. This reduced false positives due to cloud contamination and improved retrieval reliability. The injected plumes correspond to a emission rate (Q) of 10 t/h to 90 t/h in steps of 20 t/h, representative of large-scale emission events. The initial wind speed prescribed in the simulation was 5 m/s; however, during the selected snapshot used for retrieval evaluation, the near-surface wind speed across the simulation grid was approximately 3–4 m/s. These conditions reflect a favorable yet realistic scenario for geostationary methane plume detection.

Reference Datasets for Source Attribution To support the spatial attribution of detected methane plumes: The Oil and Gas Infrastructure Mapping (OGIM) dataset (Omara et al., 2023) was used to identify known anthropogenic sources such as compressor stations and flaring sites near the observed plumes. The IMEO Plume List (available at Eye on Methane data platform, `https://methanedata.unep.org/`), curated by the UNEP's International Methane Emissions Observatory, provided a benchmark reference for known high-emission locations and typical flux magnitudes observed globally. These datasets helped corroborate the retrieval results and assess source plausibility.

The acquisition times of all datasets used for both retrieval and background reference are summarized in Table 1.

Table 1: Acquisition times for methane plume and reference imagery from FCI and VIIRS sensors used in this study.

Platform	**Plume Date/UTC**	**Reference Date/UTC**
MTG-FCI (sim.)	2023-09-29 / 13:10	2023-09-30 / 13:10
MTG-FCI (real)	2023-09-29 / 10:40–15:50	2023-09-30 / 10:40–15:50
VIIRS JPSS-1	2023-09-29 / 12:24	2023-09-28 / 12:42
VIIRS JPSS-2	2023-09-29 / 12:42	2023-09-30 / 12:24
VIIRS Suomi-NPP	2023-09-29 / 11:30, 13:12	2023-09-30 / 12:54

3 Results

3.1 General Retrieval Performance

3.1.1 End-to-End simulation Assessment

Figure 3 presents a set of methane plume simulations on FCI data and their corresponding radiative impact using WRF-LES modeling and the MBMP retrieval. The RGB composite in panel (a) delineates the study region in Algeria on September 29, 2023, where high-resolution modeling of methane dispersion was conducted within the marked simulation area. The statistical distribution shown in panel (b) represents enhancement levels under plume-free conditions, indicating the background variability in the absence of simulated methane. The standard deviation ($\sigma = 0.15$) of this distribution defines a detection threshold, as enhancements exceeding 2σ are generally considered distinguishable from background noise.

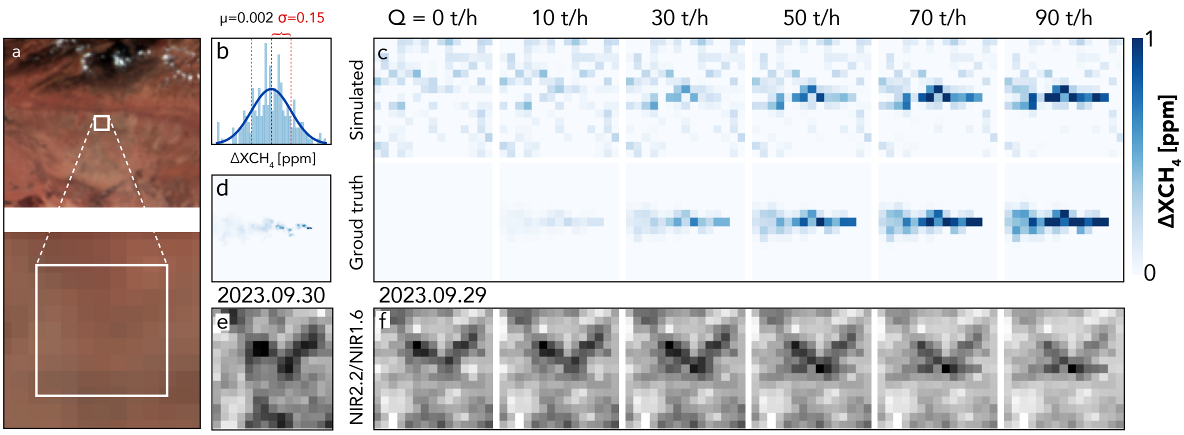

Figure 3: (a) RGB composite of the study region, with the white box indicating the simulation area. (b) Statistical distribution of the enhancement map under plume-free conditions (no simulated methane). (c) Simulated ΔX_{CH_4} (ppm) at different emission rates, where the top row represents simulated observations, and the bottom row shows the WRF-LES ground truth after convolution to $\sim$ 500 m resolution. (d) High-resolution WRF-LES methane distribution (ΔX_{CH_4}, ppm) at 25 m resolution. (e) Background radiance ratio (NIR2.2/NIR1.6) used in the retrieval. (f) Simulated variations in the radiance ratio (NIR2.2/NIR1.6) for different methane emission rates.

Panel(c) illustrates the simulated ΔX_{CH_4} in ppm across different emission rates, from 10 to 90 t/h in steps of 20 t/h. The top row corresponds to real FCI data including simulated plumes, whereas the bottom row presents the ground truth from WRF-LES simulation after convolution to $\sim$ 599 m resolution (the typical GSD in Algeria area, obtained from Figure 1a). The results indicate that for emission rates below 30 t/h, enhancement signals remain weak and are difficult to distinguish from background variability. However, starting from 30–50 t/h, MTG-FCI retrievals show noticeably enhanced plumes with greater spatial coherence, making detection increasingly reliable. This suggests that MTG-FCI's methane detection capability becomes effective within this emission range, where enhancement signals rise above background noise levels and allow for clear plume identification. The original high-resolution methane distribution from WRF-LES at 25 m resolution (panel d) provides insight into the fine-scale turbulent structures of the plume, which are partially lost in the lower-resolution retrievals due to spatial averaging effects.

Panels (e) and (f) further illustrate the spectral sensitivity to methane enhancement using the ratio of NIR2.2 to NIR1.6 radiances. Panel (e) shows the background radiance ratio under plume-free conditions, while panel (f) highlights how this radiance ratio changes in response to different methane emission rates. The methane-induced spectral contrasts become increasingly evident at higher emission intensities, demonstrating the enhanced sensitivity of the NIR2.2/NIR1.6 ratio for methane detection.

This analysis highlights the interplay between spatial resolution, enhancement signal strength, and retrieval performance. The comparison between simulated and retrieved enhancements underscores the challenge of detecting weak methane plumes while demonstrating the utility of high-resolution modeling for evaluating satellite-based retrieval techniques. Robust detection requires emissions to exceed a certain threshold relative to background noise, and retrieval algorithms must account for spatial averaging effects to ensure accurate quantification. The 10-minute temporal resolution of MTG-FCI facilitates continuous plume tracking, improving detection capabilities.

MBMP methods effectively extract methane plumes, with current detection limits in Algeria estimated at 30–50 t/h under certain illumination and wind conditions ($\tilde{3}$–4m/s per pixel on the simulation date). These results reflect best-case real-world scenarios, as the Algerian desert offers a homogeneous, dry, and highly reflective surface, and the relatively low wind speeds favored plume accumulation and visibility, which enhance detectability by reducing plume dispersion.

3.1.2 Regional Detection Capability of MTG-FCI

To evaluate the spatial variation in detection sensitivity across the full MTG-FCI disk, we also assessed the minimum detectable methane emission rate ($Q_{\min}$) under typical observational conditions. To ensure statistical significance, we selected data from three days per month between the release of MTG-FCI data in September 2024 and February 2025 (see details in Supplementary Table 1), using observations at 13:30 UTC for each selected day. The minimum $Q_{\min}$ value across all sampled data points was taken as the final result, representing the most sensitive detection threshold achievable under these conditions.

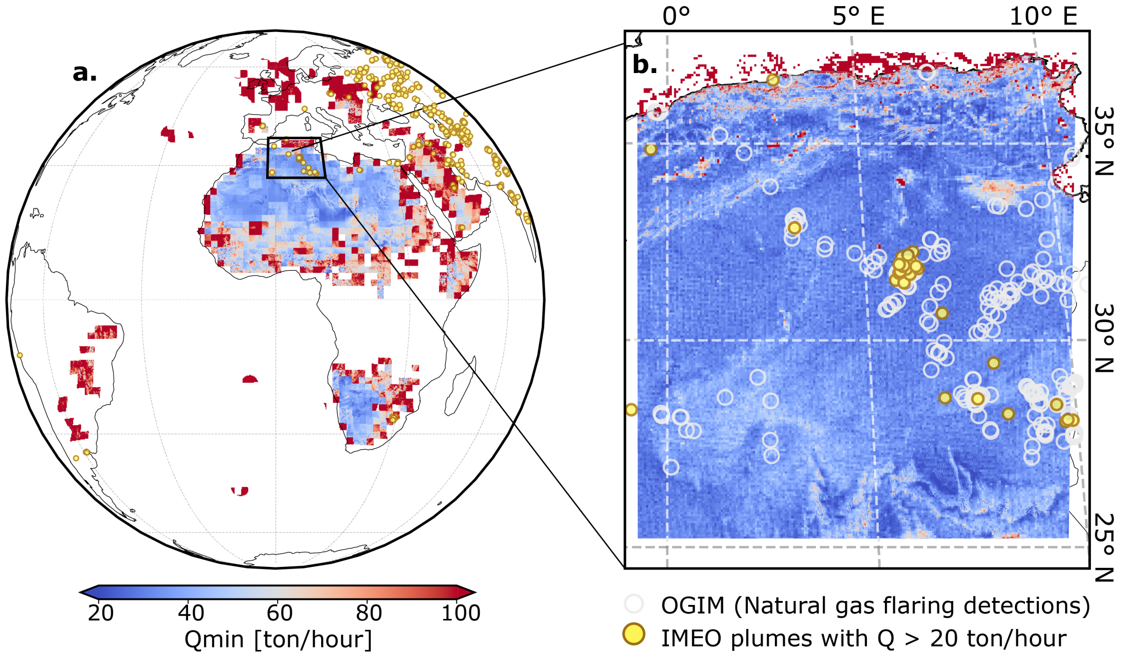

Figure 4: Overview of MTG-FCI methane detection capabilities and regional emission characterization. (a) Spatial distribution of the minimum detectable methane emission rate (Q_{min}, tons/hour) across the MTG-FCI coverage area from September 2024 to the present. Empty regions indicate cloud-masked areas derived from MSG observations. (b) Methane plume detections over the Hassi Messaoud region, overlaid with detected large-scale plumes ($Q > 20$ tons/hour, yellow) from the IMEO database and natural gas flaring locations from OGIM (white circles). This region is highlighted due to the presence of significant methane emissions observed during the analysis period.

The results presented in Figure 4 highlight the capabilities of the MTG-FCI for detecting and monitoring methane emissions at high spatial and temporal resolution. For visualization, Figure 4(a) provides an overview of regional detection capabilities at 150 km pixel resolution with statistics over a 300 × 300-pixel grid, while Figure 4(b) utilizes a finer 10 × 10-pixel grid (and 5 km gird size) to illustrate more detailed spatial variations in detection sensitivity. In ideal scenarios, such as over the Sahara, $Q_{\min}$ can reach 20 t/h, whereas the average value across the domain is considerably higher due to less favorable surface and atmospheric conditions. The resolution is highest near the satellite's nadir (Figure 1a), reaching sub-kilometer scales, while it degrades towards the periphery, where the GSD exceeds 3 km. This variation has significant implications for methane detection, as higher resolution in central regions allows for finer-scale plume identification, reducing the risk of spatial averaging that can obscure localized emissions. At higher viewing angles, methane enhancement signals tend to weaken due to increased atmospheric path length and geometric distortion, making it more challenging to detect isolated plumes. Additionally, the coarser effective resolution at oblique views can introduce further uncertainties in emission quantification and the separation of nearby sources.

Figure 4(a) illustrates the spatial distribution of Q_{min} (tons/hour) across the full MTG-FCI disk, overlaid with detected large-scale plumes ($Q > 20$ t/h) from IMEO database, revealing variations in detection sensitivity. The distribution highlights that the highest sensitivity is concentrated over regions with significant methane emissions, particularly in North Africa, the Middle East, and parts of Europe, where sources such as O&G infrastructure, industrial activities, and biogenic emissions from landfills are prominent. Conversely, regions with persistent cloud cover, particularly in the tropics and the Southern Hemisphere, exhibit reduced detection capability due to cloud interference in methane retrievals. The apparent gaps in Figure 4(a) primarily result from persistent cloudiness during the study period (September 2024 to February 2025), as well as from the limited temporal scope of the simulations. These regions were not included in the retrieval sensitivity assessment due to the lack of sufficient clear-sky scenes.

According to the IMEO database, Figure 4(b) focuses on the *Hassi Messaoud* region, a major O&G extraction hub in North Africa, recognized for its substantial methane releases (Naus et al., 2023). The detected plumes are overlaid with known flaring locations from OGIM, providing valuable context for potential emission sources.

Despite MTG-FCI's ability to achieve a minimum Q_{min} of approximately 20–30 t/h in its central coverage area, the observed methane plume activity over North Africa appears relatively sparse. While significant plumes are identified in regions like Hassi Messaoud, most of the continent shows a relatively low number of strong emissions (>10 t/h). This suggests that MTG-FCI's detection threshold may be insufficient for smaller or more diffuse sources, reinforcing its role as an effective tool for capturing major emission events rather than continuous low-intensity leaks. The statistical variability in Q_{min} between neighboring pixels, particularly in Figure 4(a), may also arise from limited valid samples per 300 × 300-pixel region or persistent cloud contamination, which inflates detection thresholds and introduces spatial discontinuities.

3.2 Case Study in Algeria

To demonstrate the capabilities of the MTG-FCI instrument for detecting transient methane emissions, we analyzed a prominent case of methane release from a compressor station in Algeria previously shown by de Jong et al. (2025), located at 34.676°N, 6.191°E. The high temporal resolution of MTG-FCI data enabled continuous monitoring of the plume's onset, growth, and dissipation, as illustrated in the time series spanning 10:40 to 15:50 UTC. To complement the MTG-FCI retrievals, we incorporated VIIRS observations from the Suomi-NPP, JPSS-1, and JPSS-2 satellites into the analysis. These data were processed using the same MBMP retrieval framework (see section 2.2). The VIIRS detections serve as supplementary snapshots during the key period of plume evolution, allowing cross-platform comparison of spatial patterns and retrieval magnitudes. In addition, external plume mass estimates reported by de Jong et al. (2025) were referenced to benchmark our emission quantification results. The corresponding IME at each time step was corrected by subtracting the contribution of the 10:40 UTC methane enhancement map (see section 2.3), integrated over the plume mask defined at the given time step. This per-mask IME correction, rare for current multispectral sensors, enhances the fidelity of the inferred emission dynamics by removing both static background contributions and potential retrieval artifacts.A comprehensive visualization of the methane plume development is provided in Figure 5. Panel (a) illustrates the spatiotemporal evolution of the plume using RGB composites and methane enhancement overlays from MTG-FCI and VIIRS, with VIIRS detections highlighted in red-outlined frames. Panel (b) identifies the emission source overlaid on Sentinel-2 imagery acquired on September 30, 2023. Panel (c) presents the temporal trends of IME (black dots-line), plume size (blue line), and the IME subtracted from the enhancement map at 10:40 UTC (grey dot-line). The typical IME baseline correction values range from 0 to 80 tons, depending on plume extent and radiance background. On top of it, the red cross markers indicate the estimations of the plume mass derived from VIIRS by de Jong et al. (2025).

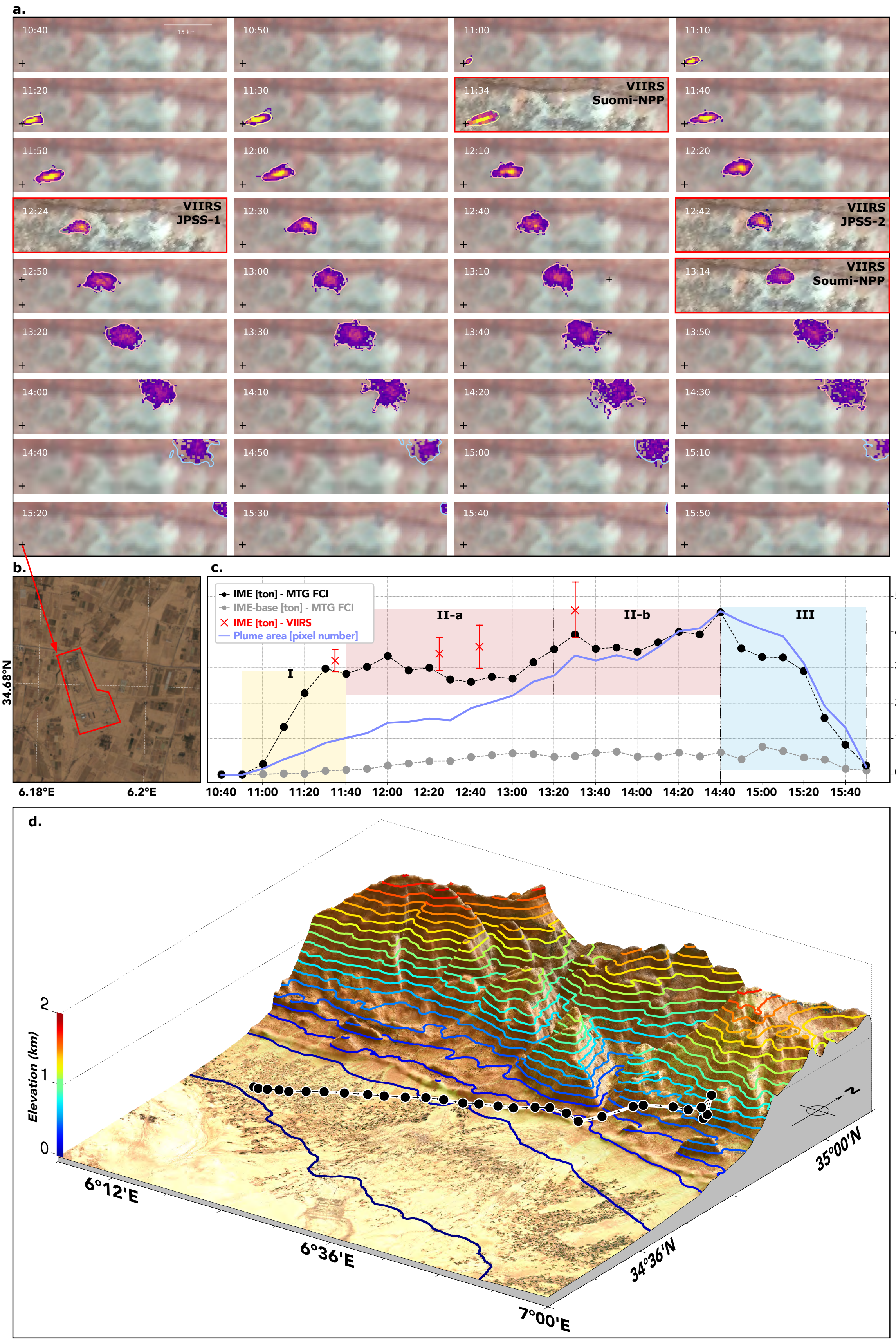
a.
b.
c.
d.
VIIRS
Suomi-NPP
VIIRS
JPSS-1
VIIRS
JPSS-2
VIIRS
Soumi-NPP
ΔXCH4 [ppm]
IME [ton] - MTG FCI
IME-base [ton] - MTG FCI
IME [ton] - VIIRS
Plume area [pixel number]
I
II-a
II-b
III
34.68°N
6.18°E
6.2°E
Elevation (km)
6°12'E
6°36'E
7°00'E
34°36'N
35°00'N

Figure 5

Figure 5. (a) Time series of RGB composites over the emission site between 10:40 and 15:50 UTC on 29 September 2023, showing methane plume retrievals from MTG-FCI and VIIRS (panels with red outlines). (b) Sentinel-2 image of the site on 30 September 2023, with the emission facility outlined in red. (c) Temporal evolution of integrated mass enhancement (IME, black dots-line) and plume area (blue line). Grey dots-line represent the IME baseline. Red crosses indicate independent IME estimates from VIIRS retrievals by de Jong et al. (2025). Shaded regions indicate distinct phases of plume evolution (I–III). (d) Three-dimensional terrain with elevation contours (100m interval); black dots show plume centerline.

As shown in Figure 5(a), the methane plume exhibits a dynamic temporal evolution characterized by variations in intensity and spatial distribution. The plume initially appears as a compact feature near the emission source and progressively disperses downwind, aligning with the prevailing wind conditions. Areas with elevated $\Delta X_{\mathrm{CH_4}}$ are highlighted using a color map range of 0-3 ppm, allowing for a clear visualization of concentration gradients. Throughout the observation period, the plume remains detectable in multiple frames. The emission site marked in Figure 5(b), delineated by the red polygon (black cross in 5(a) due to the lower GSD), corresponds to a known compressor station, which corroborates the source of the detected plume. The spatial alignment between the methane plume and the facility strengthens the validity of MTG-FCI's capability in pinpointing localized methane emissions. A visual comparison of the IME of VIIRS and MTG-FCI is presented in Figure 5(c). The VIIRS-based IME estimates (red markers) were independently calculated by de Jong et al. (2025) using a threshold-based plume masking method that did not incorporate wind data. This discrepancy likely arises from differences in spatial coverage, viewing geometry, SRF, and potentially differing auxiliary inputs (e.g., masking thresholds) used during retrieval. Although our FCI-derived IME values are slightly lower, the temporal evolution and trends remain broadly consistent with the VIIRS-derived results, reinforcing the reliability of the MTG-FCI retrieval methodology.

Based on the plume morphology observed in Panel (a) and the IME trends shown in Panel (c), the release event is segmented into three distinct phases, emitting (yellow, II), stabilization and accumulation (red, further divided into II-a and II-b), and dispersion (blue, III). These phases are also indicated by the colored plume contours in Figure 5(a) for visual reference.

The first of these, Phase I (10:50-11:40 UTC), marks the initial emitting stage. During this period, IME rises steadily from 0 to approximately 300 tons, indicating a sustained and active methane release. The plume remains compact and close to the source (black cross), suggesting that the emission dominates over dispersion, with early signs of advection beginning to stretch it along the prevailing wind direction. This phase is dominated by local accumulation and limited downwind transport.

Phase II (11:40–14:40 UTC) represents the stabilization and accumulation stage, during which the plume detaches from the source and evolves under atmospheric transport. To capture the temporal variability within this period, we further divide it into Phase II-a (11:40–13:20 UTC) and Phase II-b (13:20–14:40 UTC).

Phase II-a is a transitional phase during which the plume detaches from the source. While IME stabilizes around 250–350 tons, the plume area increases significantly from about 100 to over 250 pixels. This decoupling of IME and plume area implies that horizontal transport and mixing become the dominant processes, redistributing methane in the downwind direction without substantial additional emissions. This expansion, coupled with the steady IME, implies that the methane is no longer accumulating at the release point but is undergoing redistribution through atmospheric mixing and advection.

The relative stability of IME during this phase makes it suitable for estimating the total emitted mass.

In Phase II-b, both the IME and plume area increase again despite the cessation of emissions at the source, which might initially suggest retrieval artifacts. However, the VIIRS-based IME estimates during this interval show a similar upward trend, supporting the hypothesis that the increase may reflect a real accumulation of methane. In particular, during this time, the plume reaches the area's northern edge, where topography begins to rise into a mountain region. This orographic boundary may have hindered horizontal dispersion and promoted localized accumulation vertically, contributing to the observed IME enhancement. Therefore, although an increase in IME is observed during Phase II-b, it may not solely originate from the initial release of Phase I. Instead, it could partly result from terrain-induced accumulation. To further examine this terrain-related effect, Figure 5(d) overlays the detected plume trajectory on a three-dimensional elevation map. The black dots marks the center of the plume, which moves toward the north and reaches a region where the elevation rises sharply. This topographic barrier may have slowed horizontal dispersion and led to methane building up in place, contributing to the higher IME seen during this period. As a result, Phase II-b is not suitable for direct emission quantification, since part of the signal likely reflects terrain-driven accumulation rather than new emissions. The consistency between MTG-FCI and VIIRS-based IME estimates further supports this interpretation.

Phase III (14:40–15:50 UTC) corresponds to the dispersion stage. During this period, the IME and plume area both decline, indicating plume dilution within the boundary layer. The reduction in IME suggests that methane is no longer accumulating and is instead dispersing and mixing with the atmosphere vertically and horizontally. As the concentration approaches the detection limit, retrieval uncertainty also increases. Therefore, Phase III is also excluded from emission quantification.

To estimate Q, we use the average IME during Phase II-a, which follows the initial growth and precedes possible terrain-induced effects. Assuming a steady emission during Phase I, we calculate:

$$Q = \frac{\overline{\mathrm{IME}}_{\text{II-a}}}{\Delta t_{\mathrm{I}}} \tag{7}$$

where Q represents the average methane emission rate (t/h), $\overline{\mathrm{IME}}_{\text{II-a}}$ is the mean accumulated IME during the stabilization phase (294 ± 27 tons), and Δt_{I} is the duration of the initial emission phase (50 ± 10 minutes). The uncertainty in Q is computed using standard error propagation:

$$\sigma_Q = Q \cdot \sqrt{\left(\frac{\sigma_{\mathrm{IME}}}{\overline{\mathrm{IME}}}\right)^2 + \left(\frac{\sigma_{\Delta t}}{\Delta t}\right)^2} \tag{8}$$

Applying this to our case yields an estimated methane emission rate of: $Q = 353 \pm 78\,\mathrm{t/h}$. This result aligns well with the independent VIIRS-based estimate of 340 ± 50 t/h (de Jong et al., 2025), highlighting a significant short-term release of methane into the atmosphere.

4 Conclusion and Outlooks

This study demonstrates the capabilities of the MTG-FCI instrument for methane plume detection, quantification, and dynamic tracking under realistic conditions. Through an integrated evaluation involving end-to-end simulations, regional detection limit analysis, and a real transient emission event, we provide a robust assessment of MTG-FCI's performance for geostationary methane monitoring.

Simulation experiments using WRF-LES plume fields reveal that the current retrieval framework (MBMP) is capable of detecting methane emissions above 30–50 t/h under typical atmospheric conditions in Algeria. This detection range represents a realistic lower bound for local applications, given the spatial resolution and signal dilution associated with MTG-FCI's pixel footprint. Complementing this, the regional detection limit analysis across the MTG-FCI disk shows that the minimum detectable emission rate is approximately 20–30 t/h in central regions with favorable viewing geometry and surface conditions. These results provide operational thresholds for large-scale monitoring and source screening across Europe, Africa, the Middle East, and parts of South America.

This study also presents a real-world demonstration of MTG-FCI's capabilities using commissioning-phase data from 29 September 2023, when a transient methane release from a compressor station in Algeria was detected and dynamically tracked. The observed plume lifecycle—from onset to dispersion—was successfully captured, with the emission rate estimated at 353 ± 78 t/h. This event was independently confirmed by concurrent VIIRS observations from Suomi-NPP, JPSS-1, and JPSS-2 (de Jong et al., 2025), providing a rare opportunity to validate the retrieval performance under operational conditions. The consistency between MTG-FCI and VIIRS results supports the robustness of the MBMP algorithm and the reliability of image-based IME quantification. Moreover, continuous sampling at 10-minute intervals allowed for segmentation of the plume evolution into three distinct phases, enabling a detailed analysis of emission-driven growth versus transport-dominated dispersion dynamics.

The temporal resolution of MTG-FCI (10 minutes) is a key differentiator relative to existing polar-orbiting platforms. While satellites such as EMIT, PRISMA, and GHGSat offer high sensitivity and spatial resolution, their revisit intervals limit their capacity to characterize short-lived or intermittent emission events. In contrast, MTG-FCI enables near-continuous daytime tracking, making it especially suited for capturing transient releases due to equipment malfunction or maintenance venting. The ability to observe emission dynamics in near real-time enhances source attribution and provides actionable information to drive rapid mitigation efforts.

MTG-FCI complements other geostationary missions such as GOES-ABI, which provides similar temporal capabilities but covers the Americas region exclusively. Together, MTG-FCI and GOES extend geostationary methane monitoring coverage across different continents, offering the potential for global-scale tracking of emission events when combined with sun-synchronous observations. Furthermore, Himawari-8, covering the Asia-Pacific region, adds to this emerging network of geostationary platforms, laying the foundation for truly global, high-frequency methane monitoring. Additionally, MTG-FCI's dual sensitivity to both radiative enhancement and thermal signatures holds possibilities for detecting incomplete combustion during flaring events, offering a new avenue for evaluating flare efficiency in operational environments. In summary, MTG-FCI serves as an integral component of the global methane monitoring architecture. Its high-temporal coverage, regional coverage complements other geostationary satellites, and spectral configuration collectively enable effective detection and quantification of large emission events from geostationary orbit. These capabilities are particularly valuable for near-real-time alert systems, emission reporting verification and consistency, and targeted field response.

Future improvements should focus on reducing retrieval noise through adaptive filtering techniques, developing robust automated algorithms for methane plume detection, and exploring the synergy between geostationary and polar-orbiting observations for improved temporal and spatial coverage. Synergistic analysis across instruments will enhance the spatial and temporal completeness of methane monitoring, supporting science-based policy interventions and emissions reduction strategies.

5 Acknowledgement

We gratefully acknowledge that this work was partially performed within the framework of EUMETSAT contract 23/225824. We also thank the EUMETSAT team for their valuable support and provision of MTG-FCI commissioning-phase data, which enabled this study.

References

Aplyer, . Gefolki: Optical flow based image registration. `https://github.com/aplyer/gefolki`. Accessed: September 16, 2024.

Davis, N.N., Badger, J., Hahmann, A.N., Hansen, B.O., Mortensen, N.G., Kelly, M., Larsén, X.G., Olsen, B.T., Floors, R., Lizcano, G., et al., 2023. The global wind atlas: A high-resolution dataset of climatologies and associated web-based application. Bulletin of the American Meteorological Society 104, E1507–E1525.

Durand, Y., Hallibert, P., Wilson, M., Lekouara, M., Grabarnik, S., Aminou, D., Blythe, P., Napierala, B., Canaud, J.L., Pigouche, O., et al., 2015. The flexible combined imager onboard mtg: from design to calibration, in: Sensors, systems, and next-generation satellites XIX, SPIE. p. 963903.

Ehret, T., De Maziere, M., Hasekamp, O., Landgraf, J., 2022. Global methane monitoring using multispectral satellites. Atmospheric Measurement Techniques 15, 987–1001.

Etminan, M., Myhre, G., Highwood, E., Shine, K., 2016. Radiative forcing of carbon dioxide, methane, and nitrous oxide: A significant revision of the methane radiative forcing. Geophysical Research Letters 43, 12–614.

Frankenberg, C., Thorpe, A.K., Thompson, D.R., Hulley, G., Kort, E.A., Vance, N., Borchardt, J., Krings, T., Gerilowski, K., Sweeney, C., et al., 2016. Airborne methane remote measurements reveal heavy-tail flux distribution in four corners region. Proceedings of the national academy of sciences 113, 9734–9739.

Gorroño, J., Sanchez-Garcia, E., Irakulis-Loitxate, I., Varon, D., Guanter, L., 2023. Understanding methane emissions from multispectral satellite data. Remote Sensing of Environment 285, 113415.

Guanter, L., Irakulis-Loitxate, I., Gorroño, J., Sánchez-García, E., Cusworth, D.H., Varon, D.J., Cogliati, S., Colombo, R., 2021. Mapping methane point emissions with the prisma spaceborne imaging spectrometer. Remote Sensing of Environment 265, 112671.

Hall, J., Schroeder, W., Rishmawi, K., Wooster, M., Schmidt, C., Huang, C., Csiszar, I., Giglio, L., 2023. Geostationary active fire products validation: Goes-17 abi, goes-16 abi, and himawari ahi. International Journal of Remote Sensing 44, 3174–3193.

Holmlund, K., Grandell, J., Schmetz, J., Stuhlmann, R., Bojkov, B., Munro, R., Lekouara, M., Coppens, D., Viticchie, B., August, T., et al., 2021. Meteosat third generation (mtg): Continuation and innovation of observations from geostationary orbit. Bulletin of the American Meteorological Society 102, E990–E1015.

Jacob, D.J., Turner, A.J., Maasakkers, J.D., Sheng, J., Sun, K., Liu, X., Chance, K., Aben, I., McKeever, J., Frankenberg, C., 2016. Satellite observations of atmospheric methane and their value for quantifying methane emissions. Atmospheric Chemistry and Physics 16, 14371–14396.

de Jong, T.A., Maasakkers, J.D., Irakulis-Loitxate, I., Randles, C.A., Tol, P., Aben, I., 2025. Daily global methane super-emitter detection and source identification with sub-daily tracking. Geophysical Research Letters 52, e2024GL111824.

Myhre, G., Shindell, D., Bréon, F.M., Collins, W., Fuglestvedt, J., Huang, J., Koch, D., Lamarque, J.F., Lee, D., Mendoza, B., 2013. Anthropogenic and natural radiative forcing. Climate Change 2013: The Physical Science Basis. Contribution of Working Group I to the Fifth Assessment Report of the Intergovernmental Panel on Climate Change , 659–740.

Naus, S., Maasakkers, J., Gautam, R., Omara, M., Stikker, R., Veenstra, A., Nathan, B., Irakulis-Loitxate, I., Guanter, L., Pandey, S., et al., 2023. Assessing the relative importance of satellite-detected methane superemitters in quantifying total emissions for oil and gas production areas in algeria. Environmental Science & Technology 57, 19545–19556.

Omara, M., Gautam, R., O'Brien, M., Himmelberger, A., Franco, A., Meisenhelder, K., Hauser, G., Lyon, D., Chulakadaba, A., Miller, C., et al., 2023. Developing a spatially explicit global oil and gas infrastructure database for characterizing methane emission sources at high resolution. Earth System Science Data Discussions 2023, 1–35.

Pandey, S., Gautam, R., Houweling, S., Aben, I., Monteil, G., Nechita-Banda, N., et al., 2023. Daily monitoring of methane emissions using sentinel-3 slstr. Atmospheric Chemistry and Physics 23, 12345–12360.

Qu, Z., Jacob, D., Shen, L., Lu, X., Zhang, Y., Scarpelli, T., et al., 2021. Global methane emissions from oil and gas. Environmental Research Letters 16, 064018.

Roger, J.C., Vermeulen, A., Ciais, P., Broquet, G., Pison, I., Ramonet, M., et al., 2024. High-resolution methane mapping using enmap. Remote Sensing of Environment 300, 113845.

Saunois, M., Stavert, A.R., Poulter, B., Bousquet, P., Canadell, J.G., Jackson, R.B., Raymond, P.A., Dlugokencky, E.J., Houweling, S., Patra, P.K., 2020. The global methane budget 2000–2017. Earth System Science Data 12, 1561–1623. doi:10.5194/essd-12-1561-2020.

Schwietzke, S., Sherwood, O.A., Bruhwiler, L.M., Miller, J.B., Etiope, G., Dlugokencky, E.J., Michel, S.E., Arling, V.A., Vaughn, B.H., White, J.W., et al., 2016. Upward revision of global fossil fuel methane emissions based on isotope database. Nature 538, 88–91.

Shindell, D.T., Faluvegi, G., Walsh, M., Anenberg, S.C., Van Dingenen, R., Muller, N.Z., Austin, J., Koch, D.M., Milly, G., 2012. Simultaneously mitigating near-term climate change and improving human health and food security. Science 335, 183–189. doi:10.1126/science.1210026.

Thorpe, A.K., Frankenberg, C., Thompson, D.R., Duren, R.M., Aubrey, A.D., Bue, B.D., Green, R.O., Gerilowski, K., Krings, T., Borchardt, J., et al., 2017. Airborne doas retrievals of methane, carbon dioxide, and water vapor concentrations at high spatial resolution: application to aviris-ng. Atmospheric Measurement Techniques 10, 3833–3850.

Thorpe, A.K., Green, R.O., Thompson, D.R., Brodrick, P.G., Chapman, J.W., Elder, C.D., Irakulis-Loitxate, I., Cusworth, D.H., Ayasse, A.K., Duren, R.M., et al., 2023. Attribution of individual methane and carbon dioxide emission sources using emit observations from space. Science Advances 9, eadh2391.

UNEP, 2021. United nations environment programme (unep) report on methane emissions. UNEP .

Varon, D., Jacob, D., McKeever, J., Jervis, D., Durak, B., Xia, Y., et al., 2021. High-frequency monitoring of methane emissions using multispectral satellites. Environmental Research Letters 16, 084012.

Varon, D., McKeever, J., Jervis, D., Maasakkers, J., Pandey, S., Houweling, S., Aben, I., Scarpelli, T., Jacob, D., 2019. Satellite discovery of anomalously large methane point sources from oil/gas production. Geophysical Research Letters 46, 13507–13516.

Varon, D.J., Jacob, D.J., McKeever, J., Jervis, D., Durak, B.O., Xia, Y., Huang, Y., 2018. Quantifying methane point sources from fine-scale satellite observations of atmospheric methane plumes. Atmospheric Measurement Techniques 11, 5673–5686.

Veefkind, J., Aben, I., McMullan, K., Förster, H., de Vries, J., Otter, G., et al., 2012. Tropomi on the esa sentinel-5 precursor: A gmes mission for global observations of the atmospheric composition for climate, air quality and ozone layer applications. Remote Sensing of Environment 120, 70–83.

Watine-Guiu, M., Varon, D.J., Irakulis-Loitxate, I., Balasus, N., Jacob, D.J., 2023. Geostationary satellite observations of extreme and transient methane emissions from oil and gas infrastructure. Proceedings of the National Academy of Sciences 120, e2310797120.